arXiv:1208.3712v1 [astro-ph.SR] 18 Aug 2012

The Neptune-Sized Circumbinary Planet Kepler-38b†

Jerome A. Orosz[1], William F. Welsh[1], Joshua A. Carter[2,3], Erik Brugamyer[4], Lars A. Buchhave[5,6], William D. Cochran[4], Michael Endl[4], Eric B. Ford[7], Phillip MacQueen[4], Donald R. Short[1], Guillermo Torres[2], Gur Windmiller[1], Eric Agol[8], Thomas Barclay[9,10], Douglas A. Caldwell[9,11], Bruce D. Clarke[9,11], Laurance R. Doyle[11], Daniel C. Fabrycky[3,12] John C. Geary[2], Nader Haghighipour[13], Matthew J. Holman[2], Khadeejah A. Ibrahim[9,14], Jon M. Jenkins[9,11], Karen Kinemuchi[9,10], Jie Li[9,11], Jack J. Lissauer[9], Andrej Prša[15], Darin Ragozzine[2,7], Avi Shporer[16,17,18], Martin Still[9,10], Richard A. Wade[19]

ABSTRACT

[1]Department of Astronomy, San Diego State University, 5500 Campanile Drive, San Diego, CA 92182

[2]Harvard-Smithsonian Center for Astrophysics, 60 Garden Street, Cambridge, MA 02138

[3]Hubble Fellow

[4]McDonald Observatory, The University of Texas at Austin, Austin, TX 78712-0259

[5]Niels Bohr Institute, University of Copenhagen, Juliane Maries vej 30, 2100 Copenhagen, Denmark

[6]Centre for Star & Planet Formation, Natural History Museum of Denmark, University of Copenhagen, Øster Voldgade 5-7, 1350 Copenhagen, Denmark

[7]Astronomy Department, University of Florida, 211 Bryant Space Sciences Center, Gainesville, FL 32111

[8]Department of Astronomy, BOX 351580, University of Washington, Seattle, WA 98195

[9]NASA Ames Research Center, M/S 244-40, Moffett Field, CA 94035

[10]Bay Area Environmental Research Institute, Inc., 560 Third Street West, Sonoma, CA 95476

[11]SETI Institute, 189 Bernardo Avenue, Mountain View, CA 94043

[12]Department of Astronomy & Astrophysics, University of California, Santa Cruz, Santa Cruz, CA 95064

[13]Institute for Astronomy and NASA Astrobiology Institute University of Hawaii-Manoa, 2680 Woodlawn Dr., Honolulu, HI 96822

[14]Orbital Sciences Corporation/NASA Ames Research Center, Moffett Field, CA 94035

[15]Department of Astronomy and Astrophysics, Villanova University, 800 E Lancaster Avenue, Villanova, PA 19085

[16]Las Cumbres Observatory Global Telescope Network, 6740 Cortona Drive, Suite 102, Santa Barbara, CA 93117, USA

[17]Department of Physics, Broida Hall, University of California, Santa Barbara, CA 93106, USA

[18]Division of Geological and Planetary Sciences, California Institute of Technology, Pasadena, CA 91125

[19]Department of Astronomy & Astrophysics, The Pennsylvania State University, 525 Davey Lab, University Park, PA 16802

†Based on observations obtained with the Hobby-Eberly Telescope, which is a joint project of the University of Texas at Austin, the Pennsylvania State University, Stanford University, Ludwig-Maximilians-Universität München, and Georg-August-Universität Göttingen.

We discuss the discovery and characterization of the circumbinary planet Kepler-38b. The stellar binary is single-lined, with a period of 18.8 days, and consists of a moderately evolved main-sequence star ($M_A = 0.949 \pm 0.059\,M_\odot$ and $R_A = 1.757 \pm 0.034\,R_\odot$) paired with a low-mass star ($M_B = 0.249 \pm 0.010\,M_\odot$ and $R_B = 0.2724 \pm 0.0053\,R_\odot$) in a mildly eccentric ($e = 0.103$) orbit. A total of eight transits due to a circumbinary planet crossing the primary star were identified in the *Kepler* light curve (using *Kepler* Quarters 1 through 11), from which a planetary period of 105.595 ± 0.053 days can be established. A photometric dynamical model fit to the radial velocity curve and *Kepler* light curve yields a planetary radius of $4.35 \pm 0.11\,R_\oplus$, or $1.12 \pm 0.03\,R_{\rm Nep}$. Since the planet is not sufficiently massive to observably alter the orbit of the binary from Keplerian motion, we can only place an upper limit on the mass of the planet of $122\,M_\oplus$ ($7.11\,M_{\rm Nep}$ or $0.384\,M_{\rm Jup}$) at 95% confidence. This upper limit should decrease as more *Kepler* data become available.

1. Introduction

While the *Kepler* Mission (Borucki et al. 2010) is sometimes considered synonymous with "the search for Earth-like planets", its goals are considerably broader, and include estimating the frequency and orbital distribution of planets in multiple-stellar systems. To achieve its goals, *Kepler* relies on its exquisite photometric precision, its ability to simultaneously observe roughly 160,000 stars, and its long-duration and near-continuous time series measurements (Koch et al. 2010). This triad of unique capabilities makes *Kepler* ideally suited for exoplanet discovery and characterization, including planets in binary star systems [see Haghighipour (2010) for an in-depth discussions of planets in binary star systems].

If the binary star's orbital plane is favorably oriented, the stars will eclipse and thus reveal their binary nature. *Kepler* has discovered over 2000 eclipsing binaries (Prša et al. 2011; Slawson et al. 2011), with periods ranging from 0.075 to over 275 days, and these systems are being searched for the presence of planets. The eclipses tell us that we are viewing the binary system close to its orbital plane, and thus perhaps at a favorable orientation for finding transiting planets if the planets lie in the same orbital plane. However, detecting such planets is much more difficult than finding planets orbiting a single star. A dilution factor is present, but the main challenges arise from the fact that the transits are neither periodic nor equal in duration (e.g. see Doyle et al. 2011; Welsh et al. 2012). In addition, the deep stellar eclipses can easily mask a small transit signal. Partially compensating for these disadvantages, the timing of the eclipses of the binary component stars provides a very sensitive indicator of the presence of a third body in the system (e.g. Orosz et al. 2012). The eclipse timing variations (ETVs) as seen in an O-C diagram (Observed-minus-Computed) can reveal deviations from periodicity that are attributed to a gravitational perturbation caused by a planet. Note that for short orbital-period binaries, the ETVs are generally dominated by dynamical effects, not light-travel time delays.

The first transiting circumbinary planet discovered was Kepler-16b (Doyle et al. 2011). The transits left no room for ambiguity as to the planetary nature of the third object. The planet is in a P-type orbit (Dvorak 1984, 1986), meaning the planet is circumbinary (an outer orbit around both stars). Soon after, two more transiting circumbinary planets were discovered, Kepler-34b and Kepler-35b (Welsh et al. 2012), establishing that such planets are not rare. While there is considerable diversity among the three systems (in mass ratios, eccentricities, orbital periods), two features are in common: (i) all three planets have a radius similar to Saturn's, which is interesting in that Jupiter-radius planets should be easier to detect; and (ii) the orbital periods of the planets are only slightly longer than the minimum needed to guarantee dynamical stability according to the criteria given in Holman & Wiegert (1999). Whether this is a consequence of planet formation and migration, or simply a selection effect, is unknown.

In this paper we announce the discovery of a fourth transiting circumbinary planet, Kepler-38b. As with the other cases, the detection was made by visual inspection of a subset of the eclipsing binary star light curves, namely, those with orbital period greater than ∼1 day. The observations are presented in §2, and the photometric-dynamical model fit in §3. We conclude with a discussion in §4.

2. Observations

2.1. *Kepler* Light Curves

The details of the *Kepler* mission have been presented in Borucki et al. (2010), Koch et al. (2010), Batalha et al. (2010), Caldwell et al. (2010), and Gilliland et al. (2010) and references therein. The *Kepler* reduction pipeline (Jenkins et al. 2010a,b) provides two types of photometry, the basic simple aperture photometry (SAP), and the "pre-search data conditioned" (PDC) data in which many of the instrumental trends are removed (Smith et al. 2012; Stumpe et al. 2012). Using the PDC light curves through Q11, we conducted a visual search for small transit events in the long-period eclipsing binaries from the catalog of Slawson et al. (2011). Several candidate systems were found, including Kepler-38 (KIC 6762829, KOI-1740, 2MASS J19071928+4216451). The nominal stellar parameters listed in the Kepler Input Catalog (KIC, Brown et al. 2011) are a temperature of $T_{\rm eff} = 5640$ K, a surface gravity of $\log g = 4.47$, and apparent magnitudes of $r = 13.88$ and $Kp = 13.94$. The binary period is 18.8 days, and the eclipses are relatively shallow. The depth of the primary eclipse is $\approx 3\%$, and the depth of the secondary eclipse (which is total) is $\approx 0.1\%$.

While the PDC detrended light curves are convenient for visual searches, the detrending is not always complete. In addition, the PDC process attempts to correct for light from contaminating sources in the aperture, and correct for light lost from the target that falls outside the aperture. We have found that too much correction is sometimes applied, so we therefore use the SAP (long cadence only) light curves for the analysis that is described below. The SAP light curve was detrended in a

manner similar to what Bass et al. (2012) used. Briefly, each Quarter was treated as an independent data set. The light curve was further divided up into separate segments, using discontinuities and data gaps as end points. Splines were fit to each segment, where the eclipses and transits were masked out using an iterative sigma-clipping routine. Once satisfactory fits were found, the data were then normalized by the splines and the segments were combined. Figure 1 shows the SAP and normalized light curves. The data span 966.8 days (2.65 years) from 2009 May to 2012 January. The *Kepler* spacecraft was collecting data 92.3% of the time, and in the case of Kepler-38, 93.8% of the observations collected were flagged as normal (FITS keyword SAP_QUALITY=0).

Initially, six transit events were noticed in the light curve. These are all due to a small body transiting the primary star. The times of mid-transit, the widths, and the depths of the transits were measured by fitting a simple "U-function" (a symmetric low-order polynomial) and the results are given in Table 1. The mean period is 103.8 days. Note, however, that the transit times are poorly described by a simple linear ephemeris (see Figure 2). Furthermore, the widths of the transits depend on the binary phase, where transits that are closer to a primary eclipse (phase $\phi = 0$) are narrower than the average and transits that are closer to secondary eclipses ($\phi \approx 0.5$) are wider than the average. The large variations in the transit times and widths are a clear signature of a circumbinary object, rather than a background eclipsing binary. After a more detailed analysis was performed, two additional transits that were partially blended with primary eclipses were found, bringing the total number of transits to eight. Another transit was missed during the data download between Q7 and Q8. Figure 3 shows the transits and the best-fitting model, which is described in Section 3.1. No convincing signatures of the transits of the planet across the secondary were found in the light curve, and this point is discussed further in Section 3.1.

We also applied a novel transit search algorithm, the "Quasi-periodic Automated Transit Search" (QATS, Carter & Agol, 2012), which allows for slight variations in the inter-transit spacing. We searched through a range of periods from 50 to 300 days, and for each trial period, we computed the transit duration expected at each time in the light curve for an edge-on circular-orbiting planet. We detrended the light curve and convolved it with a boxcar with the given transit duration, and then shifted each time by the duration since (or until) the orbit would cross the barycenter of the system; this procedure makes the transit spacing and duration nearly uniform if the planet orbits with a nearly circular orbit. This algorithm detects Kepler-38b strongly with S/N ≈ 17, well above the 3σ false-alarm probability of ≈ 10. We removed the signal of Kepler-38b, re-applied the algorithm, and no other transiting bodies were detected with periods between 50 to 300 days with sizes larger than $\approx 0.7\ R_{\rm Nep}\ (P/105)^{1/2}$ at $> 3\sigma$ significance, where $R_{\rm Nep}$ is the radius of Neptune and P is the orbital period in days.

In Kepler-16, Kepler-34, and Kepler-35 the circumbinary planets gravitationally perturb the stellar orbits, leading to phase changes of the secondary eclipse relative to the primary eclipse (Doyle et al. 2011; Welsh et al. 2012). Such phase changes can be characterized by measuring accurate eclipse times for all primary and secondary eclipses, fitting a linear ephemeris using a common period and independent zero-points, and plotting the residuals on a Common Period

Observed minus Computed (CPOC) diagram. In a case such as Kepler-34 where the gravitational perturbation from the planet is relatively strong, the residuals of the primary eclipse times have a different slope than the residuals of the secondary eclipses in the CPOC diagram (Welsh et al. 2012). Over long time-scales, the phase changes become cyclic, and the signals in the CPOC diagram are poorly described by linear fits. However, if the time-scale of the observations is short compared to the precessional time-scale, then the CPOC signals of the primary and secondary will be approximately linear and fitting a linear ephemeris to the primary eclipse times and to the secondary eclipse times separately will yield different periods.

For Kepler-38, the times for the primary and secondary eclipses were measured by fitting the eclipse with a low-order cubic Hermite polynomial, as described in Steffen et al. (2011) and Welsh et al. (2012). The typical uncertainties are about 30 seconds for the primary eclipses and about 9 minutes for the secondary eclipses (see Table 2). Linear fits to the primary and secondary eclipse times were performed separately. The uncertainties on the individual times were scaled to give $\chi^2 \approx N$, where N is the number of primary or secondary eclipse times, and the following ephemerides were arrived at:

$$P = 18.7952679 \pm 0.0000029 \text{ d}, \quad T_0 = 2,454,952.872560 \pm 0.000090 \quad \text{primary}$$
$$P = 18.795224 \pm 0.000051 \text{ d}, \quad T_0 = 2,454,962.2430 \pm 0.0016 \quad \text{secondary},$$

where the times are barycentric Julian dates (BJD_TDB). The difference between these primary and secondary periods is 3.79 ± 4.40 seconds. The CPOC signals for the primary eclipses and the secondary eclipses are parallel and show no periodicities, which is an indication there are no phase changes of the secondary eclipse relative to primary eclipse. Thus the object in the circumbinary orbit in Kepler-38 has essentially no observable gravitational effect on the binary, at least on a time-scale of a few years.

2.2. High Resolution Spectroscopy

Kepler-38 was observed from the McDonald Observatory with the Harlan J. Smith 2.7 m Telescope (HJST) and the Hobby-Eberly Telescope (HET) between 2012 March 28 and May 1. The HJST was equipped with the Tull Coudé Spectrograph (Tull et al. 1995), which covers the entire optical spectrum at a resolving power of $R = 60,000$. At each visit we took three 1200-second exposures that were then co-added, assuming no Doppler shifts between them. The time of the observation was adjusted to the mid-time of the exposure, properly accounting for the CCD read-out time. The radial velocity standard star HD 182488 was usually observed in conjunction with Kepler-38. A Th-Ar hollow cathode lamp was frequently observed to provide the wavelength calibration. In all, a total of nine HJST observations of Kepler-38 were obtained. A customized IRAF script was used to reduce the data, including the correction for the electronic bias, the scattered light subtraction, the flat-field correction, the optimal aperture extraction, and the wavelength calibration. The signal-to-noise ratio at the peak of the order containing the Mg b feature near

5169 Å ranged from 10.3 to 15.9 per pixel. The HET was equipped with the High Resolution Spectrograph (HRS, Tull 1998), and the configuration we used had a resolving power of $R = 30,000$ and a wavelength coverage of about 4800 Å to 6800 Å. During each visit to Kepler-38 we also obtained a spectrum of HD 182488 and spectra of a Th-Ar lamp. A total of six observations of Kepler-38 were obtained. The images were reduced and the spectra were extracted in a manner similar to the HJST spectra, but with software customized for the HET+HRS configuration. The signal-to-noise per pixel at the peak of the order with the Mg b feature ranged from 19.4 to 45.6

We used the "broadening function" technique (Rucinski 1992) to measure the radial velocities. The broadening functions (BFs) are essentially rotational broadening kernels, where the centroid of the peak yields the Doppler shift and where the width of the peak is a measure of the rotational broadening. In order to make full use of this technique, one must have a high signal-to-noise spectrum of a slowly rotating template star observed with the same instrumentation as the target spectra. We used observations of HD182488 (spectral type G8V) for this purpose for each respective data set (HJST, HET). The radial velocity of this star was taken to be -21.508 km s^{-1} (Nidever et al. 2002).

The spectra were prepared for the BF analysis by merging the echelle orders using a two-step process. First, each order was normalized to its local continuum using cubic splines. The low signal-to-noise ends of each order were then trimmed so that there was only a modest wavelength overlap ($\approx 5 - 10\%$) between adjacent orders. The normalized orders were then co-added and interpolated to a log-linear wavelength scale. The wavelength range used in the analysis was 5137.51 to 5509.01 Å for the HJST spectra and 4830.00 to 5769.95 Å for the HET spectra.

From the BF analysis we found that the spectra were all single-lined (i.e. only one peak was evident in the BFs). Using some simple numerical simulations, we estimate that the lack of a second peak places a lower limit on the flux ratio of the two stars of $F_A/F_B \gtrsim 25$ in the HET spectral bandpass, where the subscript A refers to the brighter primary star and B refers to the fainter secondary star. A Gaussian was fit to the BF peaks to determine the peak centroids. Barycentric corrections and a correction for the template radial velocity were applied to the BF peak velocities to arrive at the final radial velocity measurements (see Table 3 and Figure 4).

The six HET spectra were Doppler corrected to zero velocity and co-added to create a "rest-frame" spectrum covering the range 4830-6800 Å. We cross-correlated this spectrum against a library of F-, G- and K-type dwarfs obtained with the HET/HRS (but with a different cross-disperser configuration). The spectrum of the G4V star HD 179958 provides a good match as shown in Figure 5.

The signal-to-noise of the spectra proved to be too low to attempt a determination of the stellar temperature, gravity, and metallicity via the measurements of individual lines. Instead, we used the Stellar Parameter Classification (SPC) code (Buchhave et al. 2012) to measure the spectroscopic parameters. The SPC analysis is well suited for spectra with relatively low signal-to-noise. The observed stellar spectrum is cross-correlated against a dense grid of synthetic spectra that consists of

51,359 models covering a wide range in effective temperatures, gravities, metallicities, and rotational velocities. Since the SPC analysis uses all of the absorption lines in the wavelength region 5050 to 5360 Å, the metallicity will be denoted as [m/H]. However, in practice we do not expect [m/H] to be significantly different from [Fe/H] for a star that is close to solar metallicity, and in the following we will consider them to be equivalent. The HJST spectra were combined to yield a spectrum with a signal-to-noise of ≈ 53 at the peak of the echelle order that contains the Mg b features near 5169 Å. The HET spectra were likewise combined to yield a spectrum with a signal-to-noise ratio of ≈ 196 near the Mg b feature. Separate fits were done with the gravity as a free parameter and with the gravity fixed at the dynamical value of $\log g = 3.926$, since the dynamically determined gravity is fairly robust and has a small uncertainty. The SPC derived parameters are given in Table 4. The gravity found by SPC agrees with the dynamical gravity at the 1σ level. The effective temperature of $T_{\rm eff} = 5623 \pm 50$ K is roughly what one expects for a spectral type of G4V. For the final adopted parameter values, we use the dynamically determined gravity, and simply average the SPC-derived values from the HJST and HET spectra with the gravity fixed.

3. Light and Velocity Curve Models

3.1. Photometric Dynamical Model

The light and velocity curves of Kepler-38 were modeled using the photometric dynamical model described in Carter et al. (2011; see also Doyle et al. 2011 and Welsh et al. 2012 for previous applications to transiting circumbinary planet systems). The code integrates the equations of motion for three bodies and, when given a reference time and viewing angle, synthesizes the light curve by accounting for eclipses and transits as necessary, assuming spherical bodies. The radial velocities of the components are also computed as a function of time. Normally, because Kepler-38 is a single-lined binary, one would have to assume a mass for the primary or assume a mass ratio to fully solve for the component masses and radii. Fortunately, the presence of transits constrain the dynamical solution since their exact timing depends in part on the binary mass ratio. On the other hand, the planet so far has had no measurable effect on the eclipse times of the primary and secondary. Given this, the stellar masses and the mass of the planet are not as tightly constrained as they were in the cases of Kepler-16, Kepler-34, and Kepler-35.

The model as applied to Kepler-38 has 34 parameters, including parameters related to the masses (the mass of Star A, the binary mass ratio, and the planetary to binary mass ratio), the stellar and planetary orbits (the period, the reference time of primary eclipse, the inclination, and eccentricity/orientation parameters), radius and light parameters (the fractional stellar radii, the planetary to primary radius ratio, the stellar flux ratios, and the limb darkening parameters), relative contaminations for each of the 11 Quarters of data, a light curve noise scaling parameter, and radial velocity zero points for the HET and HJST measurements. The model was refined using a Monte Carlo Markov Chain routine to estimate the credible intervals for the model parameters.

The resulting best-fitting parameters and their uncertainties are summarized in Table 5, and derived astrophysical parameters of interest are summarized in Table 6. Figure 3 shows the transits and the best-fitting model, and Figure 6 shows schematic diagrams of the stellar and planetary orbits.

The circumbinary planets in Kepler-16, Kepler-34, and Kepler-35 transit both the primary star and the secondary star. When transit events across both stars are observed, the constraints on the orbital parameters are much tighter than they are when only transits across the primary are seen. In the case of Kepler-38, the planet does not transit the secondary in the best-fitting model (Figure 6), although given the uncertainty in the nodal angle Ω, transits of the secondary might occur for some of the acceptable models derived from the Monte Carlo Markov Chain. However, individual transits of the planet across the secondary won't be observable, owing to the extreme flux ratio of star B to star A, where $F_B/F_A = 9 \times 10^{-4}$ in the *Kepler* bandpass (Table 5). The expected depth of the transit of the planet across the secondary is on the order of 21 ppm, which is a factor of 10 smaller than the noise level of ≈ 210 ppm. In a similar vein, occultations of the planet by star A do occur, but are undetectable given the noise level.

3.2. ELC Model

As an independent check on the parameters of the binary, we modeled the light and velocity curves using the Eclipsing Light Curve (ELC) code (Orosz & Hauschildt 2000) with its genetic algorithm and Monte Carlo Markov Chain optimizers. As noted above, we cannot use ELC to solve for the stellar masses or the absolute stellar radii since Kepler-38 is a single-lined binary. However, ELC can be used to find the orbital parameters (K, e, ω, i, P, and $T_{\rm conj}$), the fractional radii R_A/a and R_B/a, the temperature ratio T_B/T_A, and the stellar limb darkening parameters x_A and y_A for the quadratic limb darkening law $[I(\mu) = I_0(1 - x(1 - \mu) - y(1 - \mu)^2)]$. In the limiting case where the stars are sufficiently separated that their shapes are spherical, ELC has a fast "analytic" mode where the equations given in Gimenez (2006) are used. Table 7 gives the resulting parameters of the fit. The agreement between ELC and the photometric dynamical model is good.

The photometric dynamical model assumes the stars are spherical. We computed a model light curve using ELC, assuming "Roche" geometry (to the extent that is possible in an eccentric orbit, see Avni 1976 and Wilson 1979). At periastron, the "point" radius of the primary along the line of centers differs from the polar radius by 0.021%. Thus the assumption of spherical stars is a good one. The expected amplitude of the modulation of the out-of-eclipse part of the light curve due to reflection and ellipsoidal modulation is ≈ 180 ppm. If Doppler boosting (Loeb & Gaudi 2003; Zucker, Mazeh, & Alexander 2007) is included, the amplitude of the combined signal from all effects is ≈ 270 ppm, with the maximum observed at phase $\phi \approx 0.3$. Finally, the amplitude of the signal in the radial velocity curve due to the Rossiter-McLaughlin effect during the primary eclipse (when the secondary star transits the primary) is on the order of 55 m s^{-1} for a projected rotational velocity of 2.4 km s^{-1}.

4. Discussion

4.1. Planetary Parameters

The radius of Kepler-38b is $4.35\,R_\oplus$ ($= 1.12\,R_{\rm Nep}$ or $0.39\,R_{\rm Jup}$, using the equatorial radii), with an uncertainty of $\pm 0.11\,R_\oplus$ (or 2.5%). For comparison, its radius is about half of the radius of Kepler-16b ($R = 0.7538 \pm 0.0025\,R_{\rm Jup}$, Doyle et al. 2011), Kepler-34b ($R = 0.764 \pm 0.014\,R_{\rm Jup}$, Welsh et al. 2012), and Kepler 35b ($R = 0.728 \pm 0.014\,R_{\rm Jup}$, Welsh et al. 2012). Thus all four of the transiting circumbinary planets discovered so far have radii substantially smaller than Jupiter's. Since a Jupiter-sized planet would have a deeper transit and would therefore be easier to find (all other conditions being equal), the tendency for the circumbinary planets to be sub-Jupiter size is noteworthy. Pierens & Nelson (2008) argued that Jupiter-*mass* circumbinary planets in orbits relatively close to the binary should be rare owing to the various instabilities that occur during the migration phase and also to subsequent resonant interactions with the binary (Jupiter-mass circumbinary planets that orbit further out from the binary could be stable, but these would be less likely to transit owing to a larger separation). The predictions of Pierens & Nelson (2008) seem to be consistent with what is known from the first four *Kepler* transiting circumbinary planets.

Since Kepler-38b has not yet noticeably perturbed the stellar orbits, we have only an upper limit on its mass of $M_b < 122\,M_\oplus$ ($< 7.11\,M_{\rm Nep}$ or $< 0.384\,M_{\rm Jup}$) at 95% confidence. While this is clearly a substellar mass, this upper limit is not particularly constraining in terms of the density, as we find $\rho_{\rm b} < 8.18$ g cm^{-3}. A reasonable mass is $M_b \approx 21\,M_\oplus$, assuming the planet follows the empirical mass-radius relation of $M_b = (R_b/R_\oplus)^{2.06}\,M_\oplus$ (Lissauer et al. 2011).

The gravitational interaction between the planet and the two stars causes small perturbations that will grow over time and will eventually lead to a measurable change in the phase difference between the primary and secondary eclipses. As discussed above, this change in the phase difference manifests itself as a difference between the period measured from the primary eclipses and the period measured from the secondary eclipses. In Kepler-16, Kepler-34, and Kepler-35, the time-scale for a measurable period difference to occur is relatively short, as divergent periods were measured using 6 Quarters of data for Kepler-16, and 9 Quarters of data for Kepler-34 and Kepler-35. For Kepler-38, the 1σ limit on the period difference is < 4.4 seconds using 11 Quarters. Figure 7 shows the set of acceptable planetary masses and the changes in orbital period the planet would induce, based on the Monte Carlo Markov Chain from the photometric dynamical model. The larger the planetary mass, the larger the difference in periods it causes between the primary and secondary star. The lack of any measurable period difference places an upper limit on the mass of the planet: To the left of the vertical dashed line at 122 $M_\oplus$ is where 95% of the acceptable solutions reside. The vertical dot-dash line marks a planetary mass of 21 $M_\oplus$. The horizontal dashed line at 4.4 seconds marks the observed 1σ uncertainty in the measured value of $P_2 - P_1$ accumulated over the span of the current *Kepler* observations (52 binary star eclipses); valid planetary masses lie below this line, roughly. The dotted horizontal line at 0.9 seconds marks a 1σ period difference uncertainty that can be placed when ≈ 150 eclipses are eventually observed by *Kepler*, corresponding approximately

to the end of the Extended Mission in the year 2017. If no period difference is measured at that time, the mass of the planet would be less than $\approx 20\,M_\oplus$ with 1σ uncertainty. (The intersection of this period difference *uncertainty* and the 21 $M_\oplus$ line within the set of Monte Carlo points is a coincidence.) If the planet has a normal density and a mass of $21\,M_\oplus$, then the period difference would be ≈ 0.9 seconds, which would require ≈ 312 binary orbits or about 16 years to obtain a 3σ detection.

4.2. Stellar Parameters and Age

As noted earlier, the observed timing of the planet transits and the amplitude of the radial velocity curve sets the scale of the binary, and we are able to measure masses and radii for each star. Considering the fact that Kepler-38 is a single-lined spectroscopic binary (note that the ratio of the secondary-to-primary flux in the *Kepler* bandpass is 9×10^{-4}, see Table 5), the uncertainties in the masses and radii are fairly small (6.2% and 3.6% for the primary and secondary masses, respectively, and 1.8% for the radii). On the other hand, these uncertainties are still somewhat larger than what one would like when doing precise comparisons with stellar evolutionary models (for comparison, the stellar masses and radii are known to much better than 1% for the first three *Kepler* circumbinary planets, see Doyle et al. 2011 and Welsh et al. 2012). Clearly, since the radius of the primary star ($1.757 \pm 0.034\,R_\odot$) is much larger than the expected zero-age main sequence radius for its mass ($0.949 \pm 0.059\,M_\odot$), the primary must be significantly evolved, but is still a core hydrogen-burning star. The situation is shown in Figure 8, which gives the position of Kepler-38 in a $T_{\rm eff} - \log g$ diagram. The heavy solid line is a Yonsei-Yale evolutionary track (Yi et al. 2001) for [Fe/H] $= -0.11$, which is our adopted spectroscopic metallicity determination (Table 4). As indicated earlier, we assume here that the iron abundance is well approximated by the [m/H] metallicity index measured with SPC. The dark shaded area is the uncertainty in the location of the track that results from the uncertainty in the mass, and the lighter shaded area also includes the uncertainty in the metallicity. The observed $T_{\rm eff}$ and $\log g$ is just outside the 1σ region of the evolutionary track. Figure 9 shows the positions of the stars in Kepler-38 on the mass-radius and mass-temperature diagrams [the temperature of the secondary was inferred from the measured temperature of the primary (Table 4) and the temperature ratio from the ELC models (Table 7)]. They are compared against model isochrones from the Dartmouth series (Dotter et al. 2008), in which the physical ingredients such as the equation of state and the boundary conditions are designed to better approximate low-mass stars (see, e.g., Feiden et al. 2011). If we use the mass, radius, and metallicity of the primary, the inferred age is 13 Gyr. If, on the other hand, we use the measured temperature, the age of the system would be between 7 and 8 Gyr. Accounting for the small discrepancy between the measured temperature and the other parameters, we adopt an age of 10 ± 3 Gyr.

The secondary star has a relatively low mass ($0.249 \pm 0.010\,M_\odot$), and is one of just a handful of low mass stars with a well-measured mass and radius. Its mass is slightly larger than those of

CM Dra A ($0.2310\,M_\odot$; Morales et al. 2009) and KOI-126 B ($0.20133\,M_\odot$; Carter, et al. 2011), and Kepler-16b ($0.20255 \pm 0.00066\,M_\odot$; Doyle et al. 2011, see also Bender et al. 2012 and Winn et al. 2011). Stars whose mass is $< 0.8\,M_\odot$ typically have radii that are $\sim 10 - 15\%$ larger than what is predicted by stellar evolutionary models (Torres & Ribas 2002; Ribas 2006; Ribas et al. 2006; López-Morales 2007; Torres et al. 2010; Feiden et al. 2011). Relatively high levels of stellar activity induced by tidal interactions in short-period systems is one possible cause of this discrepancy (López-Morales 2007). There is a hint that the secondary star is inflated, although we note there is a small discrepancy with the models for the primary.

4.3. Stellar Variability

With *Kepler* data, it is frequently possible to determine the rotation period of the star from the modulations in the light curve due to star-spots. In the case of Kepler-38 however, the modulations are small (rms < 600 ppm for the long cadence time series, omitting the eclipses), and considerably smaller than the instrumental systematic trends in the light curve. Separating intrinsic stellar variability from instrumental artifacts is difficult, so we used the PDC light curve that has many of the instrumental trends removed. The PDC data for Kepler-38 are generally flat outside of eclipses, with the exception of Quarter 1, which we therefore omitted. The data were normalized and the primary and secondary eclipses removed from the time series. A power spectrum/periodogram was computed, and the dominant frequency present corresponds to the orbital period (18.79 days). We also patched the gaps in the light curve with a random walk and computed the auto-correlation function (ACF). The ACF revealed a broad peak at ~ 18 days, consistent with the orbital period.

The fact that the orbital period is manifest in the out-of-eclipse light curve initially suggested that star-spots were present and the star's spin was tidally locked with the orbital period. But the non-zero eccentricity of the orbit means that exact synchronicity is impossible (see below). Phase-folding the data on the orbital period, and then binning to reduce the noise, revealed the origin of the orbital modulation: Doppler boosting combined with reflection and ellipsoidal modulations. The amplitude is ~ 300 ppm with a maximum near phase $\phi = 0.25$, consistent with what is expected from the ELC models. We verified that the Doppler boost signal is also present in the SAP light curves. For more discussion of Doppler boosting in *Kepler* light curves, see Faigler & Mazeh (2011) and Shporer et al. (2011).

For an eccentric orbit, there is no one spin period that can be synchronous over the entire orbit. However, there is a spin period such that, integrated over an orbit, there is no *net* torque on the star's spin caused by the companion star. At this "pseudosynchronous" period, the spin is in equilibrium and will not evolve (Hut 1981, 1982). Given the old age of the binary, it should have reached this pseudosynchronous equilibrium state. The ratio of orbital period to pseudosynchronous spin period is a function of the eccentricity only (Hut 1981), and for Kepler-38 this period is $P_{\rm pseudo} = 17.7$ days. This is close to, but slightly shorter than, the ~ 18.79 day orbital period. Using this pseudosynchronous spin period and the measured stellar radius, a projected rotational

velocity of $V_{\rm rot} \sin i \approx 4.7$ km s^{-1} is expected, if the star's spin axis is aligned with the binary orbital axis. Our spectral modeling yields $V_{\rm rot} \sin i = 2.4 \pm 0.5$ km s^{-1}, which is close to the rotational velocity expected due to pseudosynchronous rotation. Given that the rotational velocity is near the spectral resolution limit, we can't rule out systematic errors of a few km s^{-1} caused by changes in the instrumental point-spread function, macroturbulence, etc., which could bring the measured value of $V_{\rm rot} \sin i$ up to the pseudosynchronous value.

4.4. Orbital Stability and the Habitable Zone

The 105 day planetary orbital period is the shortest among the first four *Kepler* circumbinary planets. The planet orbits the binary quite closely: the ratio of planetary to stellar orbital periods is 5.6 (ratio of semi-major axes is 3.2). Such a tight orbit is subject to dynamical perturbations, and following the analytic approximation given by Holman & Wiegert (1999), the critical orbital period in this binary below which the planet's orbit could experience an instability is 81 days. This compares favorably with the results of direct N-body integrations, which yield a critical orbit period of 75 days. Thus while stable, the planet is only 42% above the critical period (or 26% beyond the critical semi-major axis). Kepler-38 thus joins Kepler-16 (14%), Kepler-34 (21%), and Kepler-35 (24%) as systems where the planet's orbital period is only modestly larger than the threshold for stability. The fact that the first four circumbinary planets detected by *Kepler* are close to the inner stability limit is an interesting orbital feature that may be explained by processes such as planetary migration and planet-planet scattering during and/or post formation of these objects. For example, it is also possible that strong planet migration will bring planets close in: migration may cease near the instability separation leading to a pile-up just outside the critical radius; or planets that continue to migrate in are dynamically ejected, leaving only those outside the critical radius (Pierens & Nelson 2008). There is also an observational bias since objects that orbit closer to their host star(s) will be more likely to transit, making them more likely to be discovered.

Regardless of the cause, the close-to-critical orbits have an interesting consequence. Many *Kepler* eclipsing binaries have orbital periods in the range 15-50 days and have G and K type stars (Prša et al. 2011; Slawson et al. 2011), and for such binaries the critical separation (roughly 2-4 times the binary separation, depending on the eccentricity of the binary) is close to the habitable zone[1]. Thus, observed circumbinary planets may preferentially lie close to their habitable zones. Kepler-16b is just slightly exterior to its habitable zone, while Kepler-34b is slightly interior (too hot). Kepler-38b is well interior to its habitable zone, with a mean equilibrium temperature of $T_{\rm eq} = 475$ K, assuming a Bond albedo of 0.34 (similar to that of Jupiter and Saturn). Although $T_{\rm eq}$ is somewhat insensitive to the albedo, this temperature estimation neglects the atmosphere of the planet, and therefore should be considered a lower limit. It is interesting to consider the

[1]For a binary star system, the habitable zone is no longer a spherical shell but a more complex shape that rotates with the binary.

situation at a much earlier time in the past when the primary was near the zero-age main sequence. The primary's luminosity would have a factor ≈ 3 smaller, and the equilibrium temperature of the planet would have been $T_{\rm eq} \approx 361$ K, assuming a similar orbit and Bond albedo.

5. Summary

Kepler-38b is the fourth circumbinary planet discovered by *Kepler*. The planet orbits in a nearly circular 105 day orbit about an 18.8 day, single-lined eclipsing binary. Using the transits and eclipses in the light curves along with the radial velocity curve of the primary allows us to solve for the masses and radii of the two stars ($M_A = 0.949 \pm 0.059\,M_\odot$, $R_A = 1.757 \pm 0.034\,R_\odot$, $M_B = 0.249 \pm 0.010\,M_\odot$, and $R_B = 0.02724 \pm 0.0053\,R_\odot$) and the radius of the planet ($R_b = 4.35\,R_\oplus$). Since the gravitational interaction between the planet and the two stars is small, we are only able to place an upper limit of $M_b < 122\,M_\oplus$ on the mass of the planet. The first four *Kepler* circumbinary planets all have a tendency to have radii substantially smaller than Jupiter's and to have orbits that are only modestly larger than the threshold for stability. These tendencies yield clues into the formation, migration, and subsequent evolution of circumbinary planets [e.g. Meschiari (2012) and Paardekooper et al. (2012)].

Kepler was selected as the 10th mission of the Discovery Program. Funding for this mission is provided by NASA, Science Mission Directorate. JAO and WFW acknowledge support from the Kepler Participating Scientist Program via NASA grant NNX12AD23G. Support was also provided by the National Science Foundation via grants AST-1109928 to JAO, WFW, and GW, AST-0908642 to RW, AST-0645416 to EA, and AST-1007992 to GT.

REFERENCES

Avni, Y. 1976, ApJ, 209, 574

Bass, G. P., Orosz, J. A., et al. 2012, ApJ, submitted

Batalha, N. M., Borucki, W. J., Koch, D. G., Bryson, S. T., Haas, M. R., et al. 2010, ApJ, 713, L109

Bender, C. F., Mahadevan, S., Deshpande, R., Wright, J. T., Roy, A., et al. 2012, ApJ, 751, L31

Borucki, W. J., Koch, D., Basri, G., Batalha, N., Brown, T., et al. 2010, Science, 327, 977

Brown, T. M., Latham, D. W., Everett, M. E., Esquerdo, G. A. 2011, AJ, 142, 112

Buchhave, L. A., Latham, D. W., Johansen, A., Bizzarro, M., Torres, G., et al. 2012, Nature, 486, 375

Caldwell, D. A., Kolodziejczak, J. J., Van Cleve, J. E., Jenkins, J. M., Gazis, et al. 2010, ApJ, 713, L92

Carter, J. A., Fabrycky, D. C., Ragozzine, D., Holman, M. J., Quinn, S. N., et al. 2011, Science, 331, 562

Carter, J. A., & Agol, E. 2012, ApJ, in preparation

Dotter, A., Chaboyer, B., Darko, J., Kostov, V., Baron, E., & Ferguson, J. W. 2008, ApJS, 178, 89

Doyle, L. R., Carter, J. A., Fabrycky, D. C., Slawson, R. W., Howell, S. B., et al. 2011, Science, 333, 1602

Dvorak, R. 1984, Celestial Mechanics, 34, 369

Dvorak, R. 1986, A&A, 167, 379

Faigler, S. & Mazeh, T. 2011, MNRAS, 415, 3921

Feiden, G. A., Chaboyer, B., & Dotter, A. 2011, ApJ, 740, L25

Gilliland, R. L., Jenkins, J. M., Borucki, W. J., Bryson, S. T., Caldwell, D. A., et al. 2010, ApJ, 713, L160

Giménez, A. 2006, A&A, 450, 1231

Haghighipour, N. 2010, *Planets in Binary Star Systems,* (Astrophysics and Space Science Library), Vol. 366, Springer Science+Business Media B.V., Springer, Berlin

Holman, M. J. & Wiegert, P. A. 1999, AJ, 117, 621

Hut, P. 1981, A&A 99, 126

Hut, P. 1982, A&A 110, 37

Jenkins, J. M., Caldwell, D. A., Chandrasekaran, H., Twicken, J. D., Dryson, S. T., et al. 2010a, ApJ, 713, L87

Jenkins, J. M., Caldwell, D. A., Chandrasekaran, H., Twicken, J. D., Dryson, S. T., et al. 2010b, ApJ, 713, L120

Koch, D. G., Borucki, W. J., Basri, G., Batalha, N. M., Brown, T. M., et al. 2010, ApJ, 713, L79

Lissauer, J. J., Ragozzine, D., Fabrycky, D. C., Steffen, J. H., Ford, E. B., et al. 2011, ApJS, 197, 8

Loeb, A., & Gaudi, B. S. 2003, ApJ, 588, L117

López-Morales, M. 2007, ApJ, 660, 732

Meschiari, S. 2012, ApJ, 752, 71

Morales, J. C., Ribas, I., Jordi, C., Torres, G., Gallardo, J., et al. 2009, ApJ, 691, 1400

Nidever, D. L., Marcy, G. W., Butler, R. P., Fischer, D. A., & Vogt, S. S. 2002, ApJS, 141, 503

Orosz, J. A. & Hauschildt, P. H. 2000, A&A, 364, 265

Orosz, J. A., et al. 2012, ApJ, in preparation

Paardekooper, S.-J., Leinhardt, Z. M., Thebault, P. & Baruteau, C. 2012, ApJ, (in press); arXiv:1206.3484v1

Pierens, A. & Nelson, R. P. 2008, A&A, 483, 633

Prša, A., Batalha, N., Slawson, R. W., Doyle, L. R., Welsh, W. F., et al. 2011, AJ, 141, 83

Ribas, I. 2006, Ap&SS, 304, 89

Ribas, I., Morales, J. C., Jordi, C., Baraffe, I., Chabrier, G., & Gallardo, J. 2008, Mem. Soc. Astron. Italiana, 79, 562

Rucinski, S. M. 1992, AJ, 104, 1968

Shporer, A. et al. 2011, AJ, 142, 195

Slawson, R. W., Prša, A., Welsh, W. F., Orosz, J. A., Rucker, M., et al. 2011, AJ, 142, 160

Smith, J. C., Stumpe, M. C., Van Cleve, J. E., Jenkins, J. M., Barclay, T. S., et al. 2012, PASP, submitted (arX9v:1203.1383v1)

Steffen, J. H., Quinn, S. N., Borucki, W. J., et al. 2011, MNRAS, 417, L31

Stumpe, M. C., Smith, J. C., Van Cleve, J. E., Twicken, J. D., Barclay, T. S., et al. 2012, PASP, submitted (arXiv:1203.1382v1)

Torres, G. & Ribas, I. 2002, ApJ, 567, 1140

Torres, G., Andersen, J., & Giménez, A. 2010, A&A Rev., 18, 67

Tull, R. G., MacQueen, P. J., Sneden, C. & Lambert, D. L. 1995, PASP, 107, 251

Tull, R. G. 1998, Proc. SPIE, 3355, 387

Welsh, W. F., Orosz, J. A., Carter, J. A., Fabrycky, D. C., Ford, E. B. et al. 2012, Nature, 481, 475

Wilson, R. E. 1979, ApJ, 234, 1054

Winn, J. N., Albrecht, S., Johnson, J. A., Torres, G., Cochran, W. D., et al. 2011 ApJ, 741, L1

Yi, S. K., et al. 2001, ApJS, 136, 417

Zucker, S., Mazeh, T., Alexander, T. 2007, ApJ, 670, 1326

This preprint was prepared with the AAS LaTeX macros v5.2.

Table 1. Times of Planet Transit Across the Primary

N	Time (BJD - 2,455,000)	Uncertainty (minutes)	Width (days)	Depth	Binary phase
1	36.10896	14	0.825	0.0005	0.43
2[a]	140.45975	···	···	···	0.98
3	244.00847	26	0.800	0.0005	0.49
4[a]	347.73815	···	···	···	0.02
5	451.93756	18	0.884	0.0005	0.55
6[b]	555.0	···	···	···	0.04
7	659.71862	18	0.701	0.0004	0.61
8	762.33371	3	0.348	0.0004	0.07
9	867.38194	11	0.600	0.0005	0.66

[a]Transit is blended with primary eclipse.

[b]Transit is in data gap.

Table 2. Times of Primary and Secondary Eclipses

Orbital Cycle	Primary time (BJD - 2,455,000)	Uncertainty (minutes)	Orbital cycle	Secondary time (BJD - 2,455,000)	Uncertainty (minutes)
1.0	-28.33230	0.420	1.498488	-18.97115	9.303
2.0	-9.53647	0.407	2.498488	...	...
3.0	9.25767	0.420	3.498488	18.633540	8.6148
4.0	28.05360	0.434	4.498488	37.431880	10.3315
5.0	46.84874	0.434	5.498488	...	...
6.0	65.64403	0.420	6.498488	75.01589	10.218
7.0	84.43935	0.407	7.498488	...	...
8.0	103.23430	0.476	8.498488	112.59631	9.4157
9.0	122.03006	0.420	9.498488	131.39748	10.789
10.0	140.82574	0.434	10.498488	150.18989	11.383
11.0	159.62029	0.420	11.498488	168.99328	10.102
12.0	178.41584	0.434	12.498488	187.78337	9.187
13.0	197.21093	0.420	13.498488	206.58514	8.843
14.0	216.00626	0.407	14.498488	225.37215	10.216
15.0	234.80169	0.420	15.498488	244.16775	11.023
16.0	253.59677	0.420	16.498488	262.96944	10.102
17.0	272.39233	0.448	17.498488	281.75459	9.415
18.0	291.18717	0.448	18.498488	300.55308	9.650
19.0	309.98266	0.448	19.498488	319.35675	11.936
20.0	328.77848	0.434	20.498488	...	...
21.0	347.57494	0.490	21.498488	356.95425	9.529
22.0	366.36820	0.434	22.498488	375.73726	9.303
23.0	385.16363	0.420	23.498488	394.54044	10.216
24.0	403.95923	0.407	24.498488	413.32565	10.789
25.0	422.75416	0.420	25.498488	...	...
26.0	441.54956	0.434	26.498488	450.92278	10.102
27.0	460.34465	0.434	27.498488	469.71921	9.415
28.0	479.13994	0.434	28.498488	488.51035	9.873
29.0	497.93569	0.434	29.498488	507.29767	10.789
30.0	516.73073	0.420	30.498488	526.10182	9.300
31.0	535.52578	0.407	31.498488	...	...
32.0	...	...	32.498488	...	...

Table 2—Continued

Orbital Cycle	Primary time (BJD - 2,455,000)	Uncertainty (minutes)	Orbital cycle	Secondary time (BJD - 2,455,000)	Uncertainty (minutes)
33.0	573.11647	0.532	33.498488	582.48835	9.529
34.0	591.91155	0.434	34.498488	601.28219	9.187
35.0	610.70662	0.476	35.498488	620.07486	9.187
36.0	629.50191	0.420	36.498488	...	...
37.0	648.29726	0.420	37.498488	657.66824	9.873
38.0	667.09279	0.420	38.498488	676.45686	13.555
39.0	685.88782	0.420	39.498488	695.25612	10.448
40.0	704.68319	0.420	40.498488	714.05196	10.102
41.0	723.47857	0.407	41.498488	732.84697	9.415
42.0	742.27339	0.420	42.498488	751.64364	9.540
43.0	761.06937	0.420	43.498488	...	...
44.0	779.86425	0.434	44.498488	789.23446	9.758
45.0	798.65936	0.420	45.498488	808.02589	10.102
46.0	817.45492	0.420	46.498488	826.81895	10.102
47.0	836.25047	0.407	47.498488	845.61182	9.758
48.0	855.04557	0.420	48.498488	864.40410	10.448
49.0	873.84071	0.420	49.498488	883.21487	10.107
50.0	892.63578	0.434	50.498488	902.00190	9.873
51.0	911.43140	0.434	51.498488	920.80370	8.614
52.0	930.22640	0.420	52.498488	...	...

Table 3. Radial velocities of Kepler-38

Date (YYYY-MM-DD)	UT Time	BJD (−2,455,000)	RV_A (km s^{-1})	Telescope/Instrument
2012-03-28	10:43:59.63	1014.96598	19.437 ± 0.087	HJST Tull
2012-03-30	10:33:16.38	1016.95456	31.573 ± 0.067	HJST Tull
2012-03-30	10:46:45.18	1016.95524	31.526 ± 0.035	HET HRS
2012-03-31	09:48:02.35	1017.92319	34.880 ± 0.077	HJST Tull
2012-04-01	10:13:30.14	1018.94092	35.685 ± 0.062	HJST Tull
2012-04-02	10:19:00.60	1019.94478	34.998 ± 0.105	HJST Tull
2012-04-02	10:53:40.98	1019.96017	34.613 ± 0.059	HET HRS
2012-04-04	09:16:57.14	1021.90208	28.551 ± 0.059	HJST Tull
2012-04-04	10:04:33.79	1021.92614	28.148 ± 0.087	HET HRS
2012-04-05	08:37:12.35	1022.87403	24.004 ± 0.073	HJST Tull
2012-04-06	09:52:28.93	1023.92610	19.222 ± 0.112	HJST Tull
2012-04-13	09:39:44.77	1030.90929	2.272 ± 0.066	HET HRS
2012-04-25	08:22:56.79	1042.85648	18.693 ± 0.059	HET HRS
2012-04-25	09:29:11.00	1042.90247	18.565 ± 0.072	HET HRS
2012-05-01	08:50:50.33	1048.88479	0.568 ± 0.085	HJST Tull

Table 4. Spectroscopic Parameters of Kepler-38 From SPC

Parameter	HJST	HJST	HET	HET	adopted[b]
$T_{\rm eff}$ (K)	5642 ± 50	5603 ± 50	5603 ± 50	5643 ± 50	5623 ± 50
$\log g$ (cgs)	4.02 ± 0.10	3.926[a]	3.81 ± 0.10	3.926[a]	3.926 ± 0.011
[m/H] (dex)	-0.10 ± 0.08	-0.12 ± 0.08	-0.13 ± 0.08	-0.10 ± 0.08	-0.11 ± 0.08
$V_{\rm rot} \sin i$ (km s^{-1})	2.6 ± 0.5	2.6 ± 0.5	2.3 ± 0.5	2.2 ± 0.5	2.4 ± 0.5

[a]The gravity was fixed at the given value.

[b]The adopted value is the average of the HJST and HET measurements with a fixed gravity.

Table 5. Fitting Parameters for Photometric Dynamical Model

Parameter	Best fit	50%	15.8%	84.2%
Mass parameters				
Mass of Star A, M_A ($M_\odot$)	0.949	0.941	−0.059	+0.055
Mass ratio, Star B, M_B/M_A	0.2626	0.2631	−0.0056	+0.0067
Planetary mass ratio, M_b/M_A (×1000)	0.22	0.18	−0.11	+0.13
Planetary Orbit				
Orbital Period, P_b (day)	105.595	105.599	−0.038	+0.053
Eccentricity Parameter, $\sqrt{e_b}\cos(\omega_b)$	0.062	0.046	−0.064	+0.049
Eccentricity Parameter, $\sqrt{e_b}\sin(\omega_b)$	0.040	0.004	−0.100	+0.106
Time of Barycentric Transit, t_b (days since t_0)	−37.888	−37.896	−0.022	+0.044
Orbital Inclination, i_b (deg)	89.446	89.442	−0.026	+0.030
Relative Nodal Longitude, $\Delta\Omega$ (deg)	−0.012	−0.005	−0.052	+0.050
Stellar Orbit				
Orbital Period, P_1 (day)	18.79537	18.79535	−0.000051	+0.000062
Eccentricity Parameter, $\sqrt{e_1}\cos(\omega_1)$	−0.0074	−0.0074	−0.0002	+0.0002
Eccentricity Parameter, $\sqrt{e_1}\sin(\omega_1)$	−0.32113	−0.32266	−0.00188	+0.00185
Time of Primary Eclipse, t_1 (days since t_0)	−17.127434	−17.127462	−0.000078	+0.000072
Orbital Inclination, i_1 (deg)	89.265	89.256	−0.025	+0.026
Radius/Light Parameters				
Linear Limb Darkening Parameter, u_A	0.453	0.457	−0.007	+0.007
Quadratic Limb Darkening Parameter, v_A	0.143	0.135	−0.018	+0.018
Stellar Flux Ratio, F_B/F_A (×100)	0.09081	0.09059	−0.00072	+0.00071
Radius of Star A, R_A ($R_\odot$)	1.757	1.752	−0.034	+0.031
Radius Ratio, Star B, R_B/R_A	0.15503	0.15513	−0.00021	+0.00021
Planetary Radius Ratio, R_b/R_A	0.02272	0.02254	−0.00030	+0.00030
Relative Contamination, $F_{\rm cont}/F_A$ (×100)				
Quarter 1			0 (fixed)	
Quarter 2	1.40	1.37	−0.14	+0.14
Quarter 3	1.55	1.60	−0.14	+0.14
Quarter 4	1.88	1.91	−0.14	+0.14
Quarter 5	0.58	0.62	−0.14	+0.14
Quarter 6	1.21	1.17	−0.14	+0.14
Quarter 7	1.48	1.52	−0.15	+0.15
Quarter 8	1.73	1.77	−0.14	+0.14
Quarter 9	0.78	0.83	−0.14	+0.14
Quarter 10	1.26	1.25	−0.14	+0.14
Quarter 11	1.80	1.81	−0.14	+0.14
Noise Parameter				
Long Cadence Relative Width, $\sigma_{\rm LC}$ (×10^5)	17.25	17.19	−0.16	+0.16
Radial Velocity Parameters				
RV Offset, γ (km s^{-1})	18.008	17.996	−0.030	+0.031
Zero-level Diff., McDonald/HET, $\Delta\gamma$ (km s^{-1})	−0.083	−0.058	−0.035	+0.034

Note. — The reference epoch is $t_0 = 2,454,970$ (BJD).

Table 6. Derived Parameters from Photometric Dynamical Model

Parameter	Best fit	50%	15.8%	84.2%
Mass of Star A, M_A ($M_\odot$)	0.949	0.941	-0.059	$+0.055$
Mass of Star B, M_B ($M_\odot$)	0.249	0.248	-0.010	$+0.009$
Radius of Star A, R_A ($R_\odot$)	1.757	1.752	-0.034	$+0.031$
Radius of Star B, R_B ($R_\odot$)	0.2724	0.2717	-0.0053	$+0.0049$
Radius of Planet b, R_b ($R_\oplus$)	4.35	4.30	-0.11	$+0.11$
Mass of Planet b, M_b ($M_\oplus$)	< 122 (95% conf.)			
Density of Star A, ρ_A (g cm^{-3})	0.1749	0.1750	-0.0014	$+0.0014$
Density of Star B, ρ_B (g cm^{-3})	12.32	12.35	-0.25	$+0.26$
Gravity of Star A, $\log g_A$ (cgs)	3.926	3.925	-0.011	$+0.010$
Gravity of Star B, $\log g_B$ (cgs)	4.9640	4.9635	-0.0026	$+0.0026$
Fractional radius of Star A, R_A/a	0.05562	0.05560	-0.00012	$+0.00011$
Fractional radius of Star B, R_B/a	0.008623	0.008624	-0.000026	$+0.000026$
Semimajor Axis of Stellar Orbit, a_1 (AU)	0.1469	0.1466	-0.0029	$+0.0026$
Semimajor Axis of Planet b, a_b (AU)	0.4644	0.4632	-0.0092	$+0.0082$
Eccentricity of Stellar Orbit, e_1	0.1032	0.1042	-0.0012	$+0.0012$
Argument of Periapse Stellar Orbit, ω_1 (deg)	268.680	268.695	-0.039	$+0.037$
Eccentricity of Planet b Orbit, e_2	< 0.032 (95% conf.)			
Mutual Orbital Inclination[a] , I (deg)	0.182	0.191	-0.032	$+0.037$

[a]The mutual inclination is the angle between the orbital planes of the binary and the planet, and is defined as $\cos I = \sin i_1 \sin i_b \cos \Delta\Omega + \cos i_1 \cos i_b$

Table 7. Parameters from ELC Model

Parameter	Best fit
K_A (km s^{-1})	17.794 ± 0.031
e	0.1030 ± 0.0012
ω (deg)	268.68 ± 0.04
R_A/a	0.05493 ± 0.00023
R_B/a	0.00870 ± 0.00006
$T_{\rm eff,B}/T_{\rm eff,A}$	0.5896 ± 0.0026
i (deg)	89.412 ± 0.067
x_A	0.459 ± 0.027
y_A	0.130 ± 0.006
P (days)	18.7952667 ± 0.0000020
$T_{\rm conj}$ (BJD)	$2,454,971.66790 \pm 0.00005$

Note. — Note: Subscript "A" denotes the primary star, subscript "B" the secondary star.

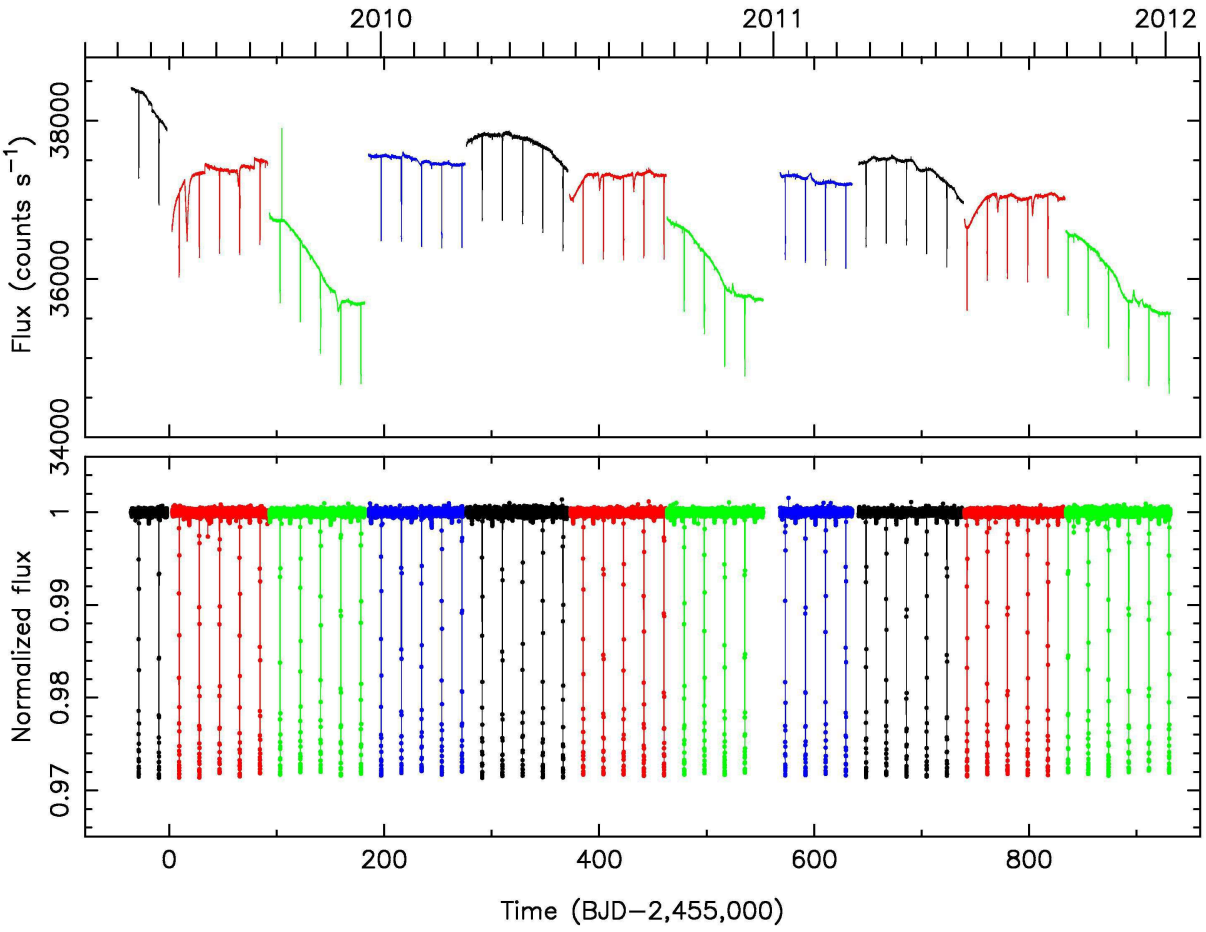

Fig. 1.— Top: the SAP light curves of Kepler-38. The colors denote the season and hence the spacecraft orientation with black for Q1, Q5, and Q9, red for Q2, Q6, and Q10, green for Q3, Q7, and Q11, and blue for Q4 and Q8. Bottom: The normalized light curve with the instrumental trends removed. One primary eclipse was missed in the relatively long interval between the end of Q7 and the start of Q8.

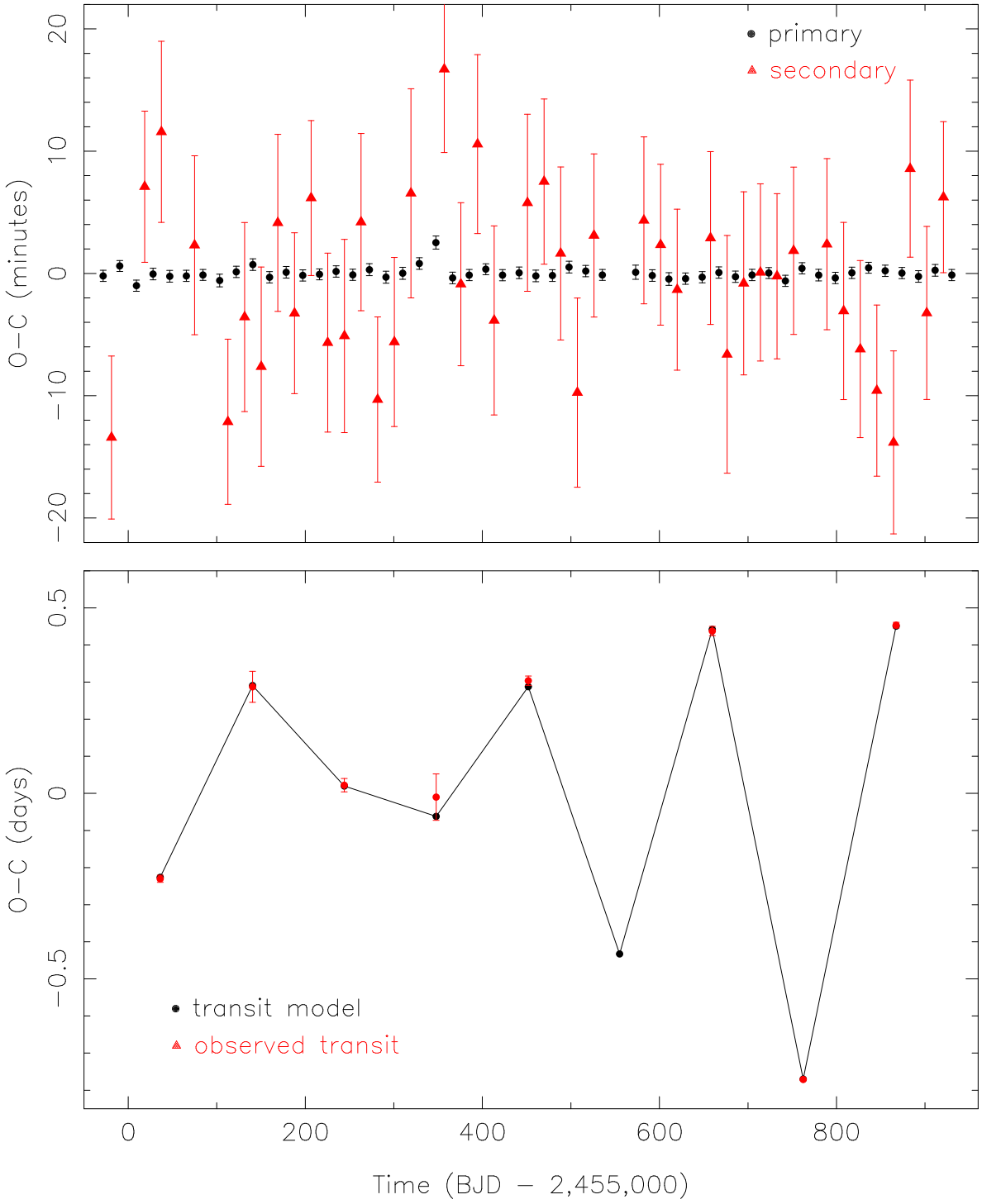

Fig. 2.— Top: O-C curves for the primary eclipses (filled circles) and secondary eclipses (filled triangles). The units on the vertical scale are minutes. No significant trends are evident. Bottom: O-C curve for the transits. Here, the units on the vertical scale are days. The large deviations from a linear ephemeris rule out a background eclipsing binary.

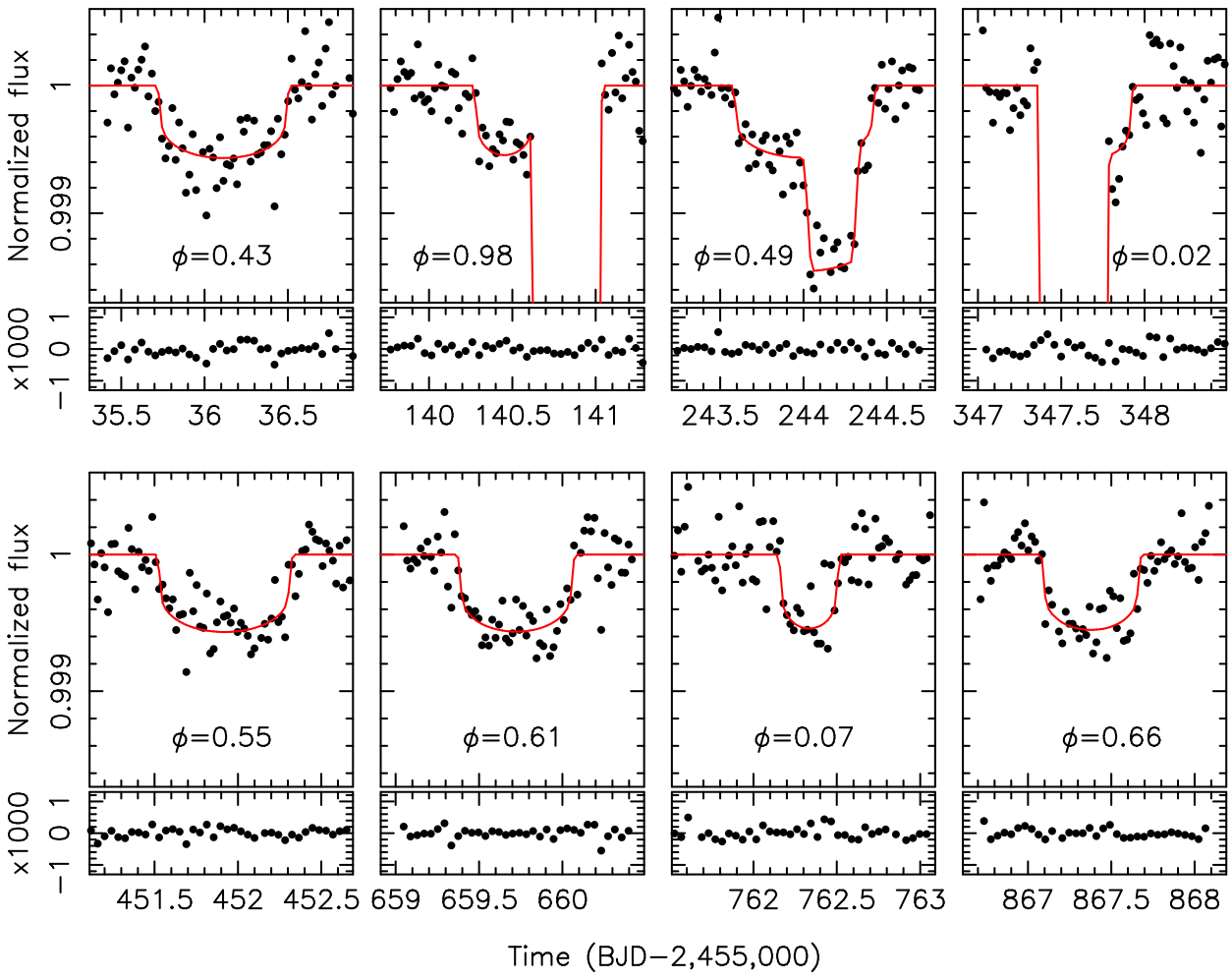

Fig. 3.— The unbinned *Kepler* light curves with the eight transit events and the best-fitting model are shown. The orbital phase of each event is indicated. Note the correlation between the width of the transit event and the orbital phase. Transits near primary eclipse ($\phi = 0$) are narrow, whereas transits near the secondary eclipse ($\phi \approx 0.5$) are wide.

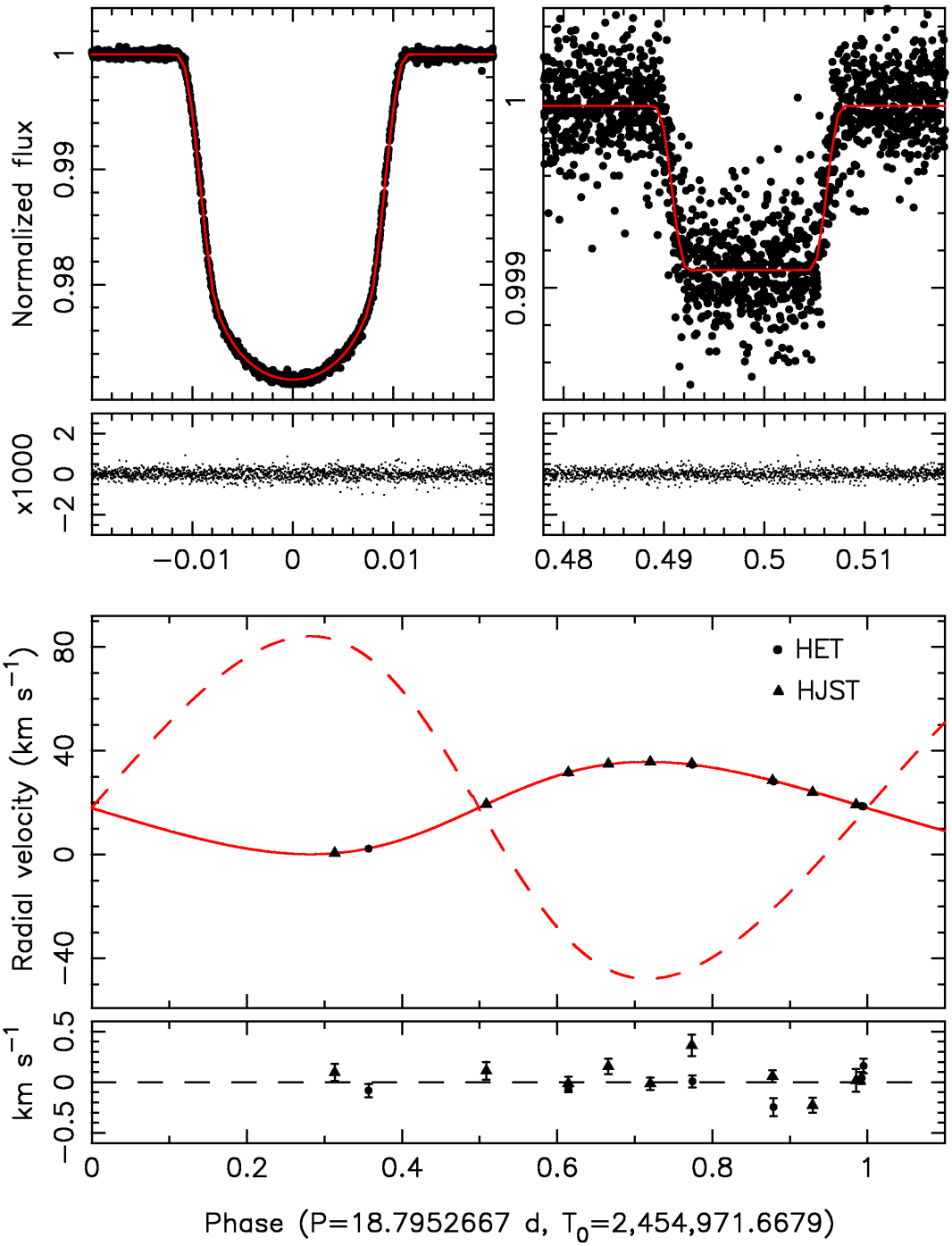

Fig. 4.— Top: The primary and secondary eclipse profiles and the ELC fits. The standard deviation of the residuals is about 210 ppm. Bottom: The radial velocities of the primary and the best-fitting ELC model curve. The dashed curve is the predicted radial velocity curve of the secondary star.

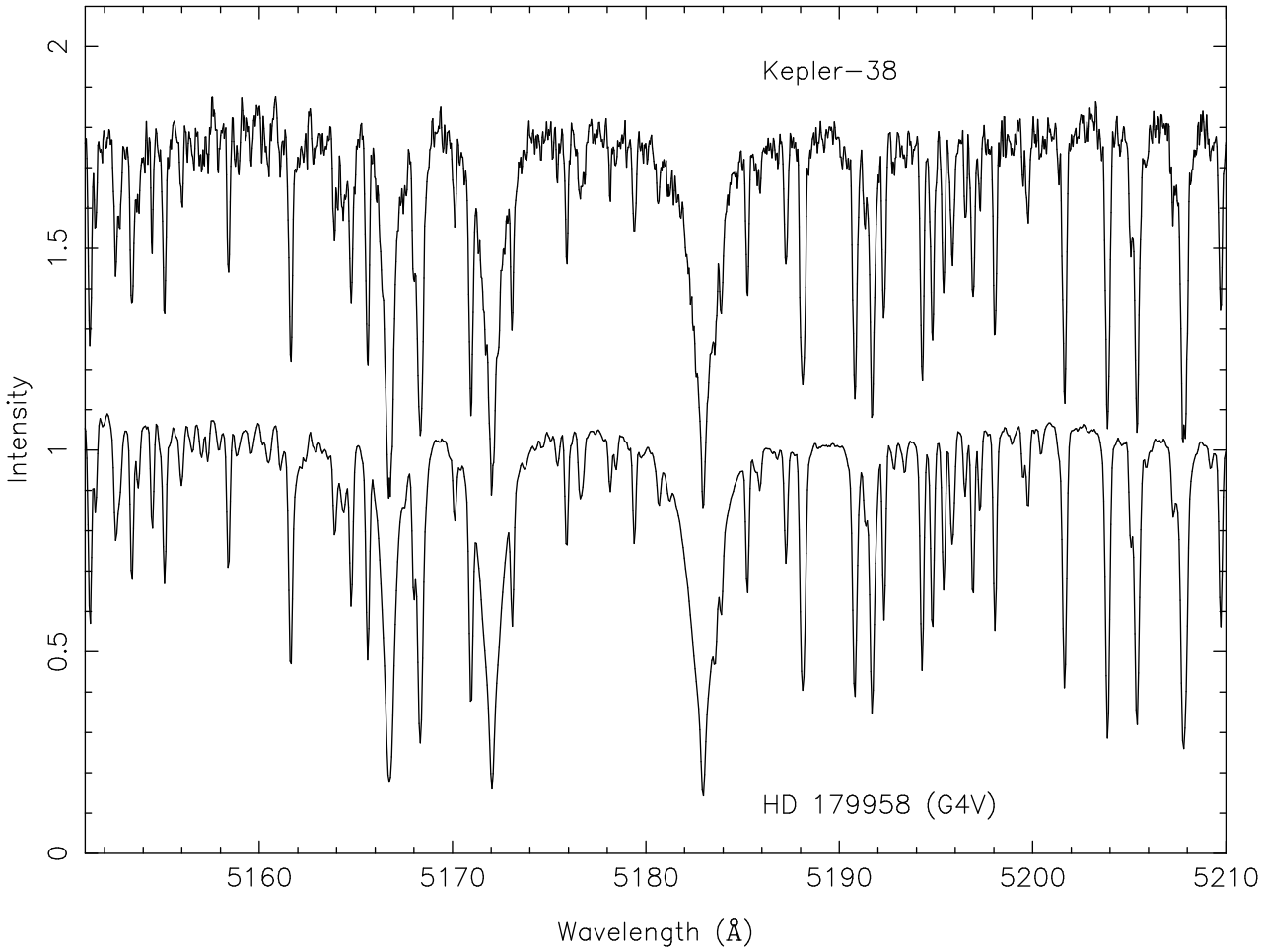

Fig. 5.— The average "restframe" HET spectrum of Kepler-38 (top, shifted vertically by 0.5 units) and the HET spectrum of the G4V star HD 179958. Overall the match is quite good.

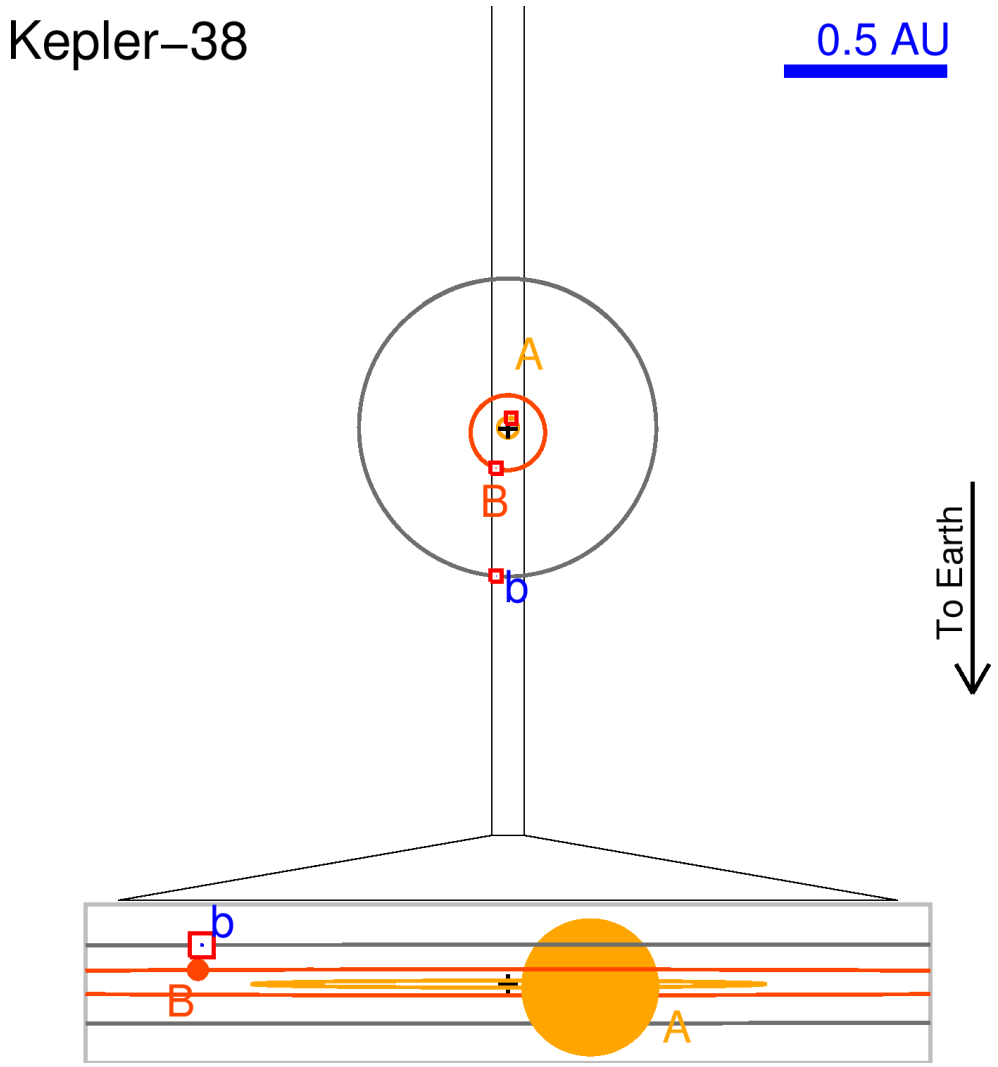

Fig. 6.— Top: A scaled, face-on view of the orbits in the Kepler-38 system is shown. The configuration shown is correct for the reference epoch given in Table 1. On this scale the stars and the planet are too small to be seen and are represented by the small boxes. The labels A, B, and b denote the primary star, the secondary star, and the planet, respectively. Bottom: The region between the vertical lines in the top diagram is shown on an expanded scale with an orientation corresponding to what would be seen from Earth. Transits of b across A are observed, and occultations of b due to A occur but are not observable given the noise level. Transits of b across B and occultations of b due to B do not occur in this configuration.

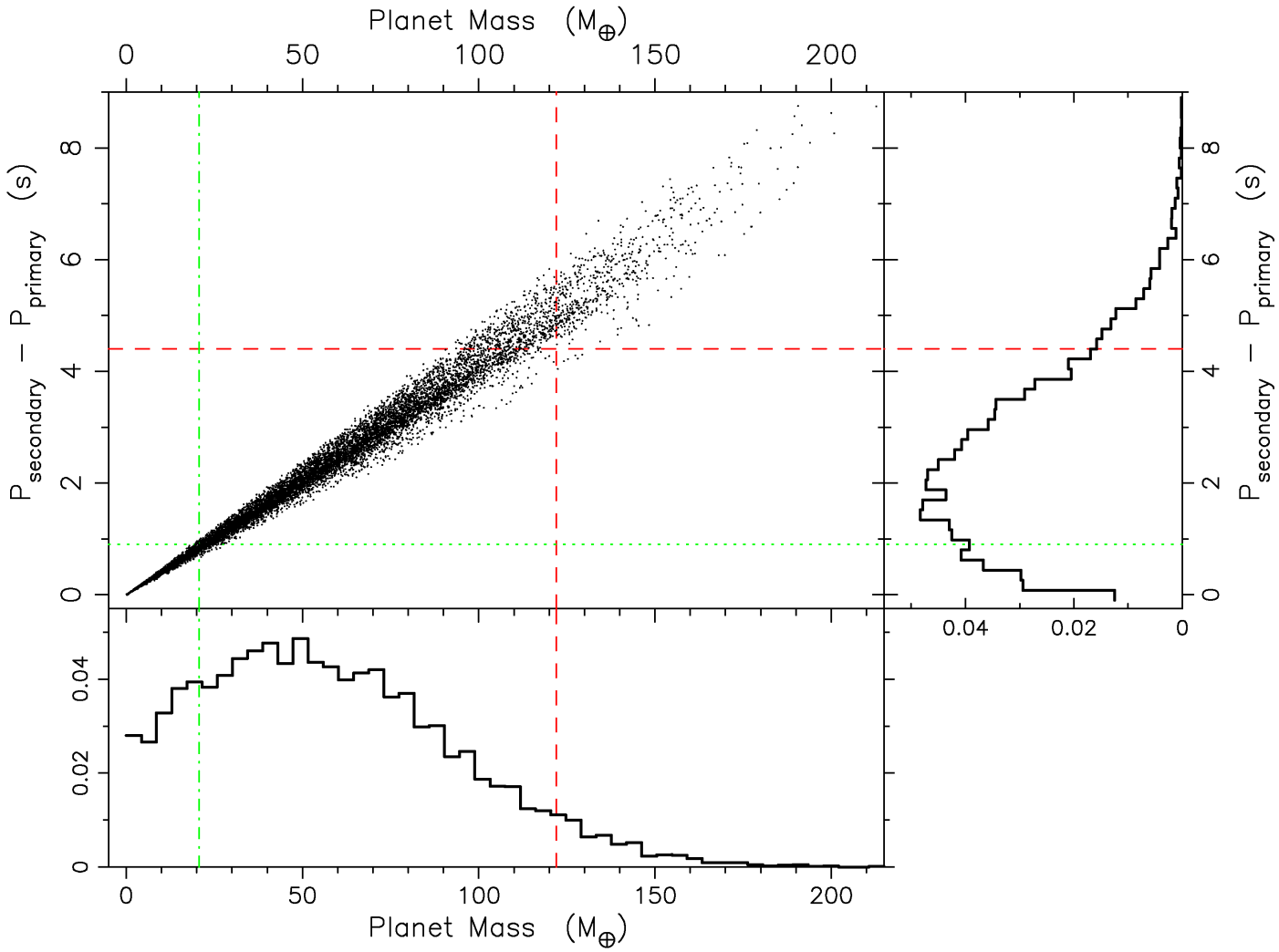

Fig. 7.— A set of 10,000 acceptable solutions from the photometric dynamical model Markov Chain Monte Carlo is plotted, showing the differences in the primary and secondary eclipse periods versus the planetary mass. Histograms of the distribution collapsed over mass and period difference are also shown, where the vertical axes represent the fraction of trials in a given bin. To the left of the vertical dashed line at $122\,M_{\oplus}$ is where 95% of the acceptable solutions are situated. The vertical dash-dotted line marks a mass of $21\,M_{\oplus}$, which is the mass the planet would have if it follows an empirical mass-radius relation. The red horizontal dashed line is the current 1σ limit of 4.4 seconds for the difference between the primary and secondary eclipse periods. The green horizontal dotted line at 0.9 seconds marks the expected location of the observational limit on the difference between the eclipse periods that should be obtainable by the end of the Extended Mission.

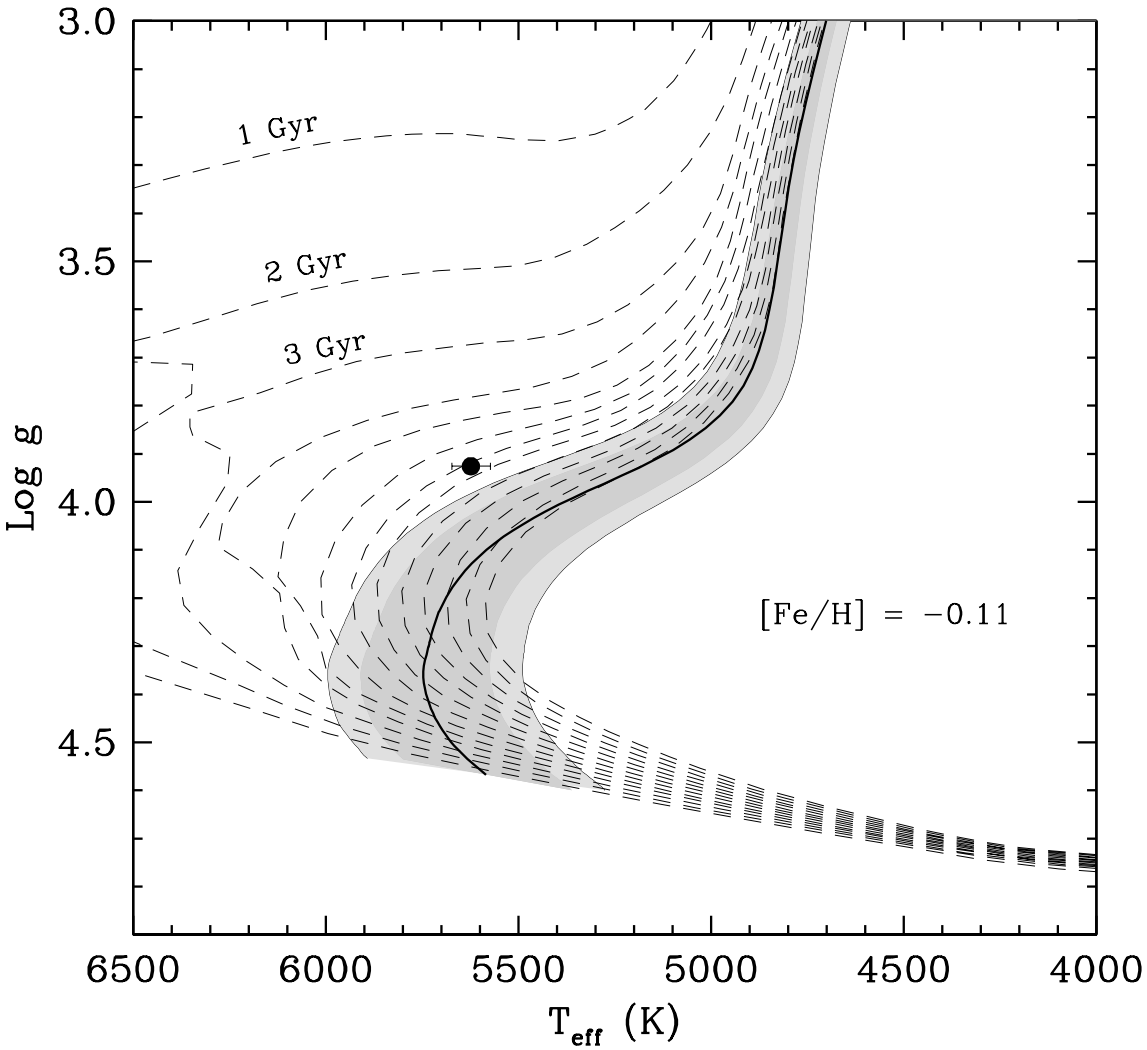

Fig. 8.— A $\log g - T_{\rm eff}$ diagram showing the location of the primary of Kepler-38 as determined from the spectroscopic analysis and the photometric dynamical model (black point). The solid line is an Yale evolutionary track appropriate for the measured mass and spectroscopic metallicity (assuming equivalency between [m/H] and [Fe/H]). The heavy shaded region shows the 1σ error region accounting for the uncertainty in the mass, and the lighter shaded region shows the 1σ uncertainty region when the uncertainty in the metallicity is also included. The dashed lines represent isochrones with the same metallicity and ages of 1–13 Gyr (left to right).

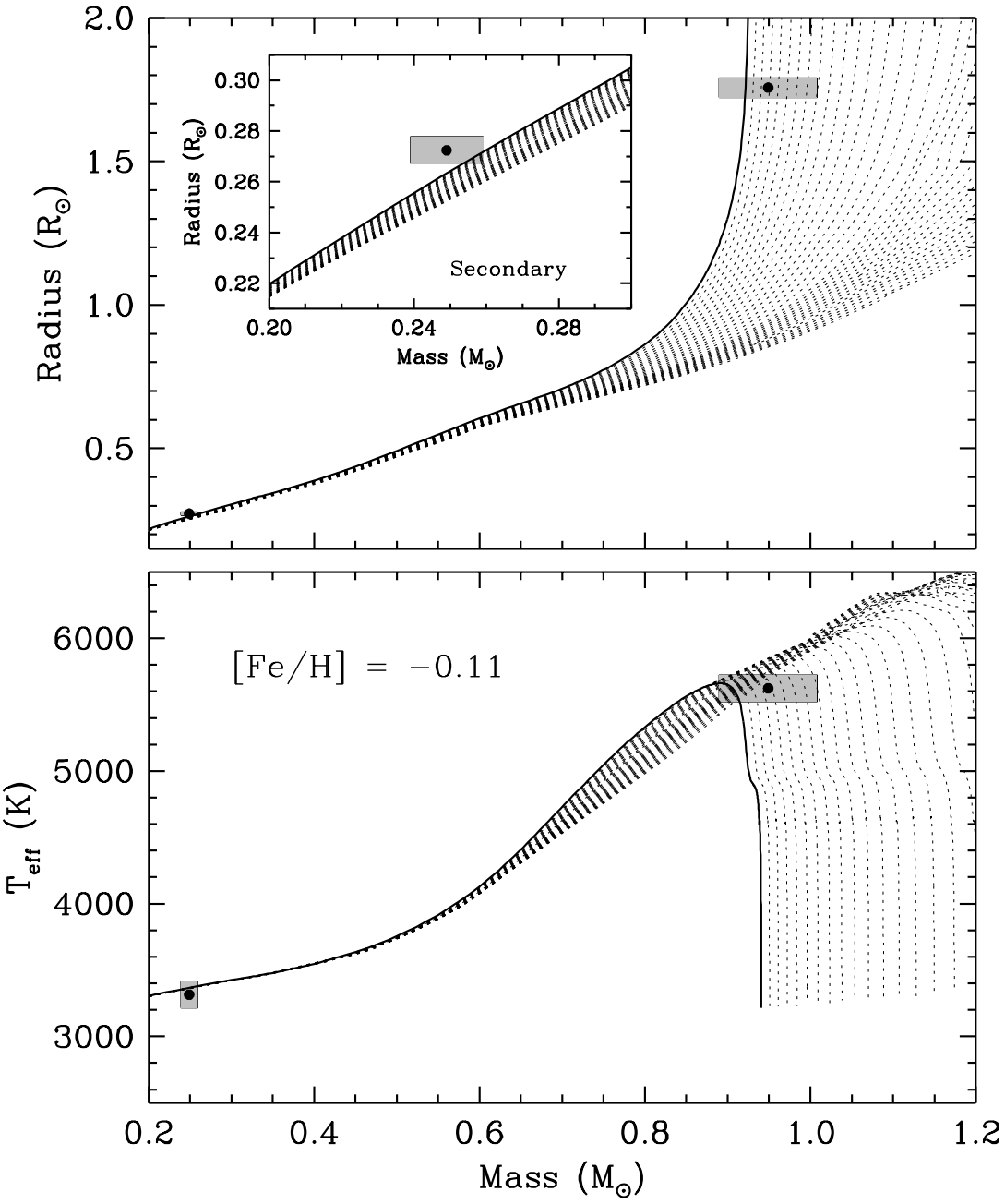

Fig. 9.— Mass-radius and mass-temperature diagrams showing the locations of the primary and secondary stars in Kepler-38. The dotted lines correspond to model isochrones from the Dartmouth series (Dotter et al. 2008) for the measured metallicity (assuming equivalency between [m/H] and [Fe/H]) and ages from 1 to 13 Gyr. The oldest isochrone is represented with a heavy solid line.